Towards the understanding of transport limitations in a proton-exchange membrane fuel cell catalyst layer: Performing agglomerate scale direct numerical simulations on electron-microscopy-based geometries

M. Barreiros Salvado, P. Schott, L. Guétaz, M. Gerard, T. David, Y. Bultel

To cite this version:

M. Barreiros Salvado, P. Schott, L. Guétaz, M. Gerard, T. David, et al.. Towards the understanding of transport limitations in a proton-exchange membrane fuel cell catalyst layer: Performing agglomerate scale direct numerical simulations on electron-microscopy-based geometries. Journal of Power Sources, 2021, 482, pp.228893 -. 10.1016/j.jpowsour.2020.228893 . hal-03492780

HAL Id: hal-03492780
https://hal.science/hal-03492780v1

Submitted on 17 Oct 2022

Version of Record: https://www.sciencedirect.com/science/article/pii/S0378775320311952
Manuscript_ae159f3d41ef2b6d95726f05d458da6b

Towards the understanding of transport limitations in a proton-exchange membrane fuel cell catalyst layer: performing agglomerate scale direct numerical simulations on electron-microscopy-based geometries

M. Barreiros Salvado[a,b], P. Schott[a,*], L. Guétaz[a], M. Gerard[a], T. David[a], Y. Bultel[b]

[a] *Univ. Grenoble Alpes, CEA, LITEN 17 Avenue des Martyrs, F-38054 Grenoble Cedex 9, France*
[b] *Univ. Grenoble Alpes, Univ. Savoie Mont Blanc, CNRS, Grenoble INP, LEPMI, F-38000 Grenoble, France*

Abstract

Improving the cathode catalyst layer design requires understanding the sources of transport limitations in proton-exchange membrane fuel cells. For the purpose, a framework consisting on an electron microscopy characterization setup in couple with a numerical modeling software is proposed. The latter integrates high-performing geometry building capabilities which ensure full phase discretization (carbon, platinum, ionomer and pore phase) and freedom when designing the structure morphology and meshing. The 3D structure of the carbon phase is extracted from a focused ion beam scanning electron microscopy analysis having a 2 nm isotropic resolution. The platinum phase is built according to a nanoparticle size histogram determined from high angle annular dark field scanning transmission electron microscopy images. To add the ionomer phase, the thickness of the layer is measured on high resolution transmission electron microscopy images. The multi-physics model includes gas transport in the pores, and gas and ionic transport in the Nafion. A 4-step reaction mechanism is used to solve the electrochemistry. Numerical simulations are performed on two catalyst layer portions. The results show that structural heterogeneities can deeply impact performance. Such impact is mainly linked to oxygen diffusion limitations through the Nafion film and, to a certain extent, to interparticle competition effects.

Keywords: PEM fuel cell, catalyst layer, electron microscopy, 3D structure reconstruction, modeling, agglomerate

---

[*] Corresponding author
Email address: `pascal.schott@cea.fr` (P. Schott)

Preprint submitted to Journal of Power Sources *13th August 2020*

1. Introduction

Prior to commercialization, proton-exchange membrane fuel cells (PEMFCs) face major challenges primarily involving cost reduction. Platinum - the catalyst used in the cathode catalyst layer (CCL) of conventional PEMFCs - is rare and costly; therefore, it is crucial to optimize its utilization.

In the case of operation at high current densities, major performance losses are commonly observed [1]. These losses have origin in the sluggish kinetics of the oxygen reduction reaction (ORR) [2, 3], oxygen transport limitations within the gas diffusion layer [1] and, both oxygen and proton transport limitations in the cathode catalyst layer [4]. The oxygen transport limitations in the cathode catalyst layer can be decoupled into those arising from the oxygen diffusion in the pores [4] and the oxygen diffusion through the ionomer thin film covering the carbon and catalyst surface [5, 6] - reportedly of significantly higher resistance to oxygen permeability than bulk ionomer [7]. While the diffusion in the pore phase is expected to have an effect when considering the whole catalyst layer thickness, the diffusion through the ionomer is expected to be limiting even at the agglomerate scale. Furthermore, an additional interfacial oxygen transport resistance in the platinum/ionomer region is reported to be the dominant factor for voltage drops at high current densities [5]. Similarly to oxygen transport resistance, an increased proton transport resistance is also observed in the thin layer comparatively to bulk ionomer [8]. Moreover, this increased resistance is reportedly associated to the ionomer's structure arrangement, which depends on the operating conditions [9], the treatment protocol [9, 10], the type of substrate interfacing [11, 12] and the layer thickness [13]. Since the transport related losses in the cathode are also strongly linked to the cathode catalyst layer microstructure, understanding the morphology and the distribution of the different CCL constituents (carbon support, Pt nanoparticles and ionomer) at a local nanoscale and quantifying their effects on the electrochemical phenomena is primordial.

Among the available tools to approach the issue, numerical modeling is commonly used to predict these effects. However, catalyst layer structure-oversimplification based on the assumption of an idealized geometry (as used in macroscale models [14, 15, 16, 17, 18]) may give rise to misleading conclusions. Moreover, agglomerate/pore-scale models have been developed, though these also mostly consist of oversimplified structures which assume agglomerates as ideally spherically-shaped [15, 16, 19, 20, 21]. These models have demonstrated to inaccurately describe the average electrochemical reaction rate [22]. Therefore, numerical modeling on real catalyst layer structures emerges as the most promising approach towards further comprehension at this scale [23].

Major improvements over recent years in microstructure characterization - based on X-ray or electron microscopy - have given access to 3D microstructures of the catalyst layer. Yet, the process of moving from characterization to modeling is not a straight path as it involves several steps: image acquisition, image treatment and geometry building. A list of image acquisition techniques based on both X-ray and electron microscopy has already been reported in the literature with the purpose of imaging the PEMFC catalyst layer [24]. On the one hand, the cathode catalyst layer is a nanocomposite material consisting of carbon nanoparticles (30-50 nm) supporting Pt nanoparticles (2-10 nm) and covered by a thin layer (5-15 nm) of ionomer binder, but on the other hand it is also a porous material with some pores larger than a hundred nanometers, and as a result, there is no single technique capable of characterizing these different length scales.

The step following the image acquisition consists in the image treatment, which is essential for electron microscopy techniques. By default, the acquisition is followed by a pretreatment phase that integrates a set of standardized procedures transversal to all images output from electron microscopy based techniques. These procedures follow the respective order: image alignment (in the case of an acquisition in series), structure reconstruction (in the case of a tomography), noise reduction and contrast enhancement (crucial steps preceding the thresholding), and segmentation [6, 25, 26, 27, 28]. In the case of FIB-SEM acquisitions, it has been found that embedding samples in epoxy resin prior to acquisition facilitates the thresholding when comparing to non-embedded samples [26, 29, 30]. Regarding the set of required post-treatment procedures to follow, there are existing softwares on the market that were either designed to perform these tasks - image alignment, noise reduction, contrast enhancement and thresholding - or had added functionalities/plug-ins over time - MATLAB® [27, 31, 32], Fiji ImageJ [25, 27, 29, 33], Avizo [34, 35, 36], DigiM [35], to name a few.

The final step is the geometry building; even latest agglomerate/pore scale models which use electron microscopy input do not exploit its full potential in the geometry building [20, 28, 36, 37, 38, 39, 40]. The commonly reported methods to reproduce CCL geometries follow either one of two ways: generating a 3D mesh out of the post-treated stack of 2D images and importing the mesh (usually .stl, .step, .vtp or .vtu format) into a CFD code-based software (Comsol ® Multiphysics, Ansys CFX and Ansys Fluent, Simcenter™ Star-CCM+®, OpenFOAM®, TRUST...) [6, 33, 36], which is a fast method though it makes it impossible to discretize the phases within. These phases include platinum, carbon, Nafion and pore phase. The other way consists in using stochastic methods either based on the QSGS algorithm [41] as used in the work of [23] or based on a 2-point correlation function extracted from TEM or FIB-SEM acquisition output [27, 42, 43]. To the best of our knowledge, the direct conversion of a 3D stack into such a CAD format remains elusive and may constitute an open subject of interest for future work.

In this work, a multiscale characterization was performed, using the following three different electron microscopy techniques: FIB-SEM, HAADF-STEM and HRTEM. A FIB-SEM resolution of 2 nm on SEM images with a slice thickness of 2 nm (a low value when compared to previous works) was attained. Such high isotropic resolution allows extracting more reliable effective transport properties that can be introduced in macrohomogeneous models, since varying the resolution from 2 to 20 nm can cause significant differences in the transport properties [6]. The FIB-SEM acquisition was used to build the carbon phase, while the platinum and Nafion phases were built according to HAADF-STEM and HRTEM respectively. Here, a non-stochastic method for the generation of 3D geometries - based on electron microscopy input with the four phases discretized - is proposed. The generation of these geometries is performed using geometry building capabilities integrated in Comsol ® Multiphysics. This approach provides notoriously more freedom regarding geometry designing than mesh importing. It opens the possibility for addition of the remaining phases, which in this case refer to the platinum nanoparticles and the Nafion thin film, as well as having full control over the morphology (shaping and size-adjusting) - e.g. Nafion distribution, platinum nanoparticle size and distribution. Numerical simulations were then carried on two geometries with an applied set of physics that integrates both transport of species (oxygen and protons) and electrochemistry. These tests showed that the effects of heterogeneities on local performance are already noticeable at this scale. These effects have origin particularly in severe oxygen transport limitations on the Nafion phase and, to a certain extent, on platinum interparticle competition effects.

2. Experimental setup

2.1. Catalyst coated membrane fabrication

The catalyst coated membrane (CCM) (7 cm x 7 cm) was built in-house. The ink was prepared by mixing a commercial Pt/C catalyst TEC10EA30E-HT (30.1% Pt/graphitized carbon) and a Nafion ® dispersion D2020 (EW=1000, DuPont™) into deionized (DI) water/propan-1-ol solvent. Initially the mixture of Pt/C and Nafion (I/C = 1) in DI water was stirred at 4000 rpm during 15 min, a process after which propan-1-ol was gradually added and mixed (water/propan-1-ol weight ratio = 4.32) prior to depositing and baking on a Teflon blank sheet. The deposition proceeded at a temperature of 40°C followed by the drying of the slurry-covered substrate over a heated table within 10 min. Subsequently, this layer was transferred onto a Nafion ® membrane NRE-211 by hot pressing (at a pressure of 3.5 MPa and a temperature of 160 °C for 3 min).

The anode and cathode catalyst layer, and membrane thicknesses were measured and the respective values were found: 8 μm, 14 μm and 25 μm. In addition, a value of 0.3 mg/cm^2 for the cathodic Pt loading was found.

For the purpose of this work, three different samples were prepared, each with the aim of characterizing a different phase within the composite electrode, as described in the following subsections.

2.2. Image acquisition

Different acquisition techniques are commonly used as a means to provide information on each phase [23, 35]. In order to 3D-image the solid phase structure (including C, Pt and ionomer), both techniques - nano-scale X-ray computed tomography (nano-XCT) [44, 45, 46] and focused ion beam - scanning electron microscopy (FIB-SEM) [6, 25, 33, 34, 47, 48, 49, 50] - are used. Nano-CT refers to a non-destructive characterization method which is limited by the low atomic number of both carbon and ionomer and by its resolution of ~ 50 nm when using commercial equipment [44, 46] and ~ 20 nm when using a synchrotron X-ray source [23]. However, this technique can 3D-image the Pt/C/Nafion agglomerates and the pores that are larger than the resolution (20-50 nm). Pore size distributions extracted from nano-CT have shown good agreement with the distributions obtained using mercury intrusion porosimetry (MIP) once considering the pores larger than 20-50 nm. The other technique - the 3D FIB-SEM - consists in successive FIB milling and SEM imaging. During the acquisition, a resolution of ~ 2 nm for the SEM images is often used [6, 47, 51, 52], whereas the thickness of the FIB slice milling is larger (often around 20–30 nm), generating a 3D image with voxels elongated in the milling direction. Such voxel anisotropy leads to the introduction of an artificial tortuosity anisotropy [6]. Regardless, a decrease in slice thickness is expected to occur with FIB improvement [30, 52]. From FIB-SEM images, pore size distributions are usually extracted. These are found to be consistent with measurements employing BET and MIP techniques, considering only pores larger than 5-10 nm (smaller pores can be an artifact generated by the SEM image noise) [6, 51, 52]. To image the platinum phase, the TEM technique - which has a resolution that can go up to 0.1 nm once a lens aberration corrector is used - is the leading technique for measuring the size distribution of Pt nanoparticles [23, 34, 52, 53, 54, 55, 56]. The small-angle X-ray scattering (SAXS) technique which generally requires a synchrotron source is less frequently used, despite its advantage of providing nanoparticle size histograms based on the analysis of a much greater number of nanoparticles [23]. Furthermore, the platinum particle distribution within an electrode containing more than 10,000 nanoparticles has been determined by performing an electron tomography acquisition on an electrode embedded in epoxy resin and cut by ultramicrotomy [35, 52]. Since TEM samples must be transparent to electrons, electron tomography experiments are then restrained to samples having a thickness in the order of ~ 100 nm. More recently, advanced electron tomography experiments carried out on Pt/C catalyst powder have determined whether Pt nanoparticles are located on the surface or within the carbon support particle [57, 58]. In particular, a detailed 3D analysis of different types of carbon supports revealed the presence of nanoscale pores (in the range of 1-20 nm) inside these primary carbon particles and showed that the predominant location of the Pt nanoparticles - either on the carbon particle surface (exterior nanoparticles) or inside the carbon particle (interior nanoparticles) - depends on the size and density of these small pores [57]. To 3D image the ionomer phase distribution within an electrode, further developments are required as it still remains extremely challenging. The difficulties behind the ionomer imaging result from the lack of contrast between the ionomer and the carbon support since these have a similar mass density, plus the ionomer forms a thin layer (few nm) that covers the carbon catalyst support. Therefore, high resolution images are required. As fluorine is one of the ionomer's main components, mapping fluorine in the electrode is a solution for imaging it. Thus, STEM/X-EDS fluorine elemental map has become commonly used to determine whether the distribution of the ionomer is homogeneous throughout the electrode [59, 60]. However, the spatial resolution of these maps is limited by the weak X-EDS signal emitted by a thin layer of ionomer and by the high sensitivity of the ionomer to electron beam radiation damage leading to a significant fluorine loss during the map acquisition [59, 61]. Among the X-ray techniques, the soft X-ray scanning transmission microscopy (STXM) using the chemical contrast associated with the near edge X-ray absorption fine structure of fluorine and carbon has also been developed to image the ionomer inside the electrode [62]. This method combined with tomography experiments has shown its ability to 3D image the electrode ionomer distribution [63, 64]. Nonetheless, the size of the X-ray probe (30 nm) and the sensitivity of the ionomer to the X-ray beam restrain the resolution of this technique which is then not high enough to image the ionomer thin layer. This thin layer was first revealed on high resolution TEM images [55, 60]. Afterwards, electron tomography experiments provided 3D images of carbon agglomerates covered with a thin layer of ionomer. In these experiments, the contrast of the ionomer was enhanced by staining the ionic domains with heavy Cs^+ ions [65]. This experiment made it possible to measure the average thickness of the ionomer thin layer (~ 7 nm) and also to determine to which extent the carbon particles were covered. In addition, the carbon particle coverage was found to increase with the ionomer content, while the ionomer thickness remained unchanged. It is worth noting that these experiments were carried out on a model active layer prepared with an ink consisting of carbon black in the absence of Pt nanoparticles since the high contrast of the platinum disturbs the 3D reconstruction of the ionomer phase. Atomic force microscopy (AFM) is also a powerful technique which can provide access to the thickness of the ultra-thin layer of ionomer [66]. Such technique - currently limited to 2D images - has the great advantage of being able to measure the ionomer thickness under different relative humidities [67].

2.2.1. FIB-SEM

Here, a small piece of the CCM was cut and pore-filled with epoxy resin. The cross-section of the embedded CCM piece was then polished mechanically until obtaining a mirror-like surface that can be observed by SEM after depositing a thin layer of carbon to enhance electron conductivity.

The image acquisition was performed on a Zeiss cross-beam 550 FIB-SEM microscope. Prior to performing the image acquisition, a Pt protective layer was deposited on the surface of the area of interest and a large hole was excavated next to this area with a high current Ga^+ beam of 30 keV. The current of the Ga^+ beam was then decreased in order to obtain a fine-polished surface. Subsequently, the Ga^+ beam was used to trench the area of interest slice by slice while SEM images of each slice were recorded using a 1 keV electron beam and an in-lens backscattered detector. In the end, a thousand images were recorded with a size of 1089*486 pixels, and therefore a voxel size of 2x2x2 nm^3. The resulting volume of the analyzed cathode portion was 2.178∗0.972∗2 μm^3. It is worth noting that the backscattered electron image of each slice contains information that belongs not only to the cutting plane but also to the following slice since the 1 keV electron beam backscatters from a depth below the surface larger than 2 nm. This resolution limit in the milling direction is highlighted in the Pt nanoparticle 3D images which instead of having a spherical shape, these present an ellipsoidal-like shape elongated in the direction perpendicular to the cutting plane. To overcome this limitation, the use of a lower electron beam accelerating voltage is required. However, this would lead to a poorer resolution and signal-to-noise ratio of the SEM images. Due to the high resolution of the SEM images, any instability (mechanical, electromagnetic, charge/heat build-up...) during the acquisition on the sample and/or on the electron beam causes 3D image distortions that are visible on the raw reconstructed stack of images. To correct these distortions, a registration procedure taking into account not only a rigid translation in the cutting plane but also non-linear deformations is required.

2.2.2. HAADF-STEM

The embedded CCM cross-section used for the FIB-SEM acquisition was also used to prepare the TEM samples by ultramicrotomy, which were required for the characterization of the Pt nanoparticles. Thin slices (~70 nm-thick) were cut using a LEICA UC6 ultramicrotome at room temperature and then deposited on a TEM copper grid.

In order to analyze the Pt nanoparticle size distribution, the thin CCM embedded cross-section was observed using a FEI-Themis microscope operated at 200 kV and equipped with a Cs probe corrector. The size of these nanoparticles was measured on images acquired at high magnification (910000X) using Fiji ImageJ software, allowing in the end to obtain a representative size histogram.

2.2.3. HRTEM

In the analysis of the Nafion thin layer covering the catalyst carbon support, an alternative method of TEM sample preparation had to be developed without using epoxy resin pore filling. Indeed, on HRTEM images, the epoxy resin and the ionomer have a similar contrast corresponding to that of an amorphous material, so it would be impossible to distinguish between both. The partial embedding method [55] has already been successfully used for the case of a thick electrode, though it becomes difficult to perform on a thinner electrode. Therefore, in this work, to the best of our knowledge, thin CCM cross-sections were prepared by cryo-ultramicrotomy (LEICA UC7 ultramicrotome) without using epoxy resin embedding for the first time. Since the small piece of CCM, even when frozen at -140 ºC, was too flexible to be cut by the diamond knife, the sample was made stiffer by embedding it into a frozen deionized water drop. To do this, a small piece of CCM was stood upright in a liquid deionized water drop that was then quenched in liquid ethane in order to freeze the water as quickly as possible. The frozen sample was transferred under cryo-atmosphere to the cryo-ultramicrotome where 250 nm-thick CCM cross-sections were cut at -140°C and then deposited on a lacey carbon TEM grid using an ionizer system. It should be noted that depositing the CCM cross-section flat on the TEM grid is the most difficult step in this cryo-ultramicrotomy process, although on most of our TEM grids it was possible to find large pieces of electrode cross section. In the end, the TEM grids were removed from the cryo-ultramicrotome and heated to room temperature so that the frozen deionized water drop could melt and finally evaporate. In the case where the ionomer distribution is not homogeneous within the electrode, preparation by cryo-ultramicrotomy appears to be a more suitable method for obtaining a representative thin electrode sample than the easier method of scraping the electrode and depositing the resulting powder on a TEM grid covered with a lacey carbon layer.

The CCM cross-section prepared by cryo-ultramicrotomy was then observed using a FEI-Titan operating at 200kV, which is both Cs probe and image corrected.

3. Image post-treatment

In this section, the post-treatment procedures on the different types of images are described. In the case of the FIB-SEM images, the backscattered electron (BSE) signal images were chosen over the secondary electron (SE) as these provided a better contrast [29]. Figure 1a shows a typical backscattered electron SEM image acquired during the FIB-SEM experiment. In this image, the highest contrast arises from the Pt nanoparticles which appear as numerous bright dots, while the carbon support presents a much lower contrast and the ionomer cannot be clearly distinguished from either the carbon support or the resin. Though, the insufficient resolution obtained in the acquisition is still preventing from solving/measuring the platinum nanoparticles. This explains why the Pt particle size characterization was not performed through a segmentation on the FIB-SEM image but rather on multiple HAADF-STEM images. However, it was still possible to isolate the solid phase from the pore phase whilst segmenting the FIB-SEM images.

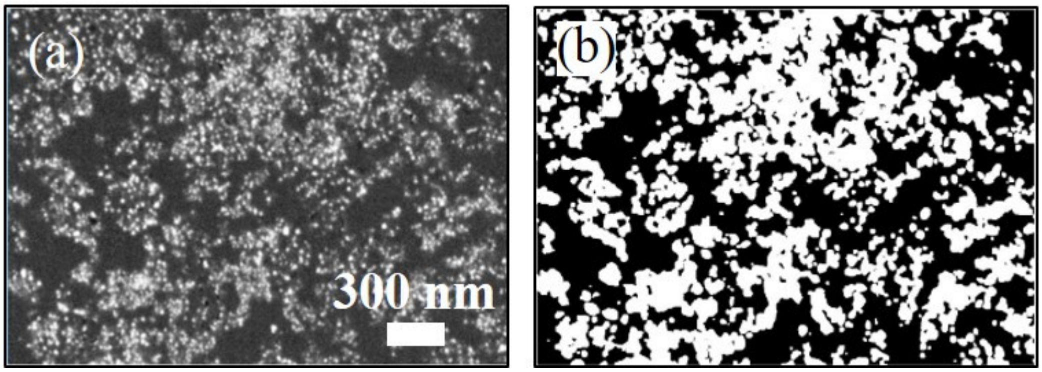

Figure 1: a) SEM image extracted from the FIB-SEM image stack. b) Corresponding segmented image.

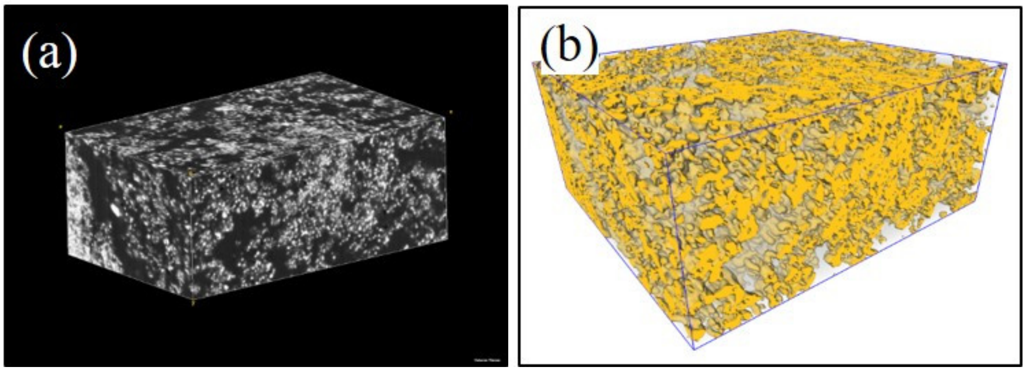

Figure 2: a) 3D view of the catalyst layer imaged with FIB-SEM ($2.178*0.972*2\ \mu m^3$). b) Corresponding segmented image stack.

Prior to segmentation, the stack of images must undergo a processing step. This processing step consists in the alignment of slices with respect to one another (stack registration), homogenization of the contrast/brightness over the entire volume, and standard image processing filters to reduce artifacts and noise on the images (such as curtaining effect induced by the FIB beam). For the image alignment, as some image deformations are observed, an alignment procedure beyond a simple linear transformation must be performed. Therefore, the alignment was performed using less restrictive operations (i.e. scaling, rotation, distortion) on Fiji ImageJ. With the images aligned, the following step in the procedure is the segmentation. This is one of the most delicate steps as it has a crucial importance when it comes to building a reliable geometry, as significant artifacts can be introduced if not correctly performed. Therefore, a set of segmentation criteria which includes pixel intensity and both texture and edge detection was defined. For the purpose, a multicriteria software based on supervised machine-learning - Ilastik [68] - was used since it provides very precise and robust results when compared to more traditional algorithms that use the gray level as the single criterion. This permitted obtaining a reliable segmented image stack. The result on a single 2D image can be seen in figures 1a and 1b, whereas the whole segmented stack is presented in figure 2b with the corresponding aligned FIB-SEM images in figure 2a.

To obtain information on the catalyst particle size distribution, multiple HAADF-STEM images are used. These were manually thresholded using Fiji ImageJ while overlaying the raw gray scale image and the segmented one. In the meantime, as these were segmented, the measured sizes were cumulatively added to a particle size histogram until the normalized distribution of particles did not change. All the measurements performed on different Pt nanoparticle images that could correspond to overlapping images of nanoparticles located at distinct heights in the sample were manually removed prior to building the nanoparticle size histogram which was based on ~ 200 particle size measurements (fig. 3b).

Here, an average platinum particle size (diameter) value of 4.5 nm was found which is similar to the one reported by [58].

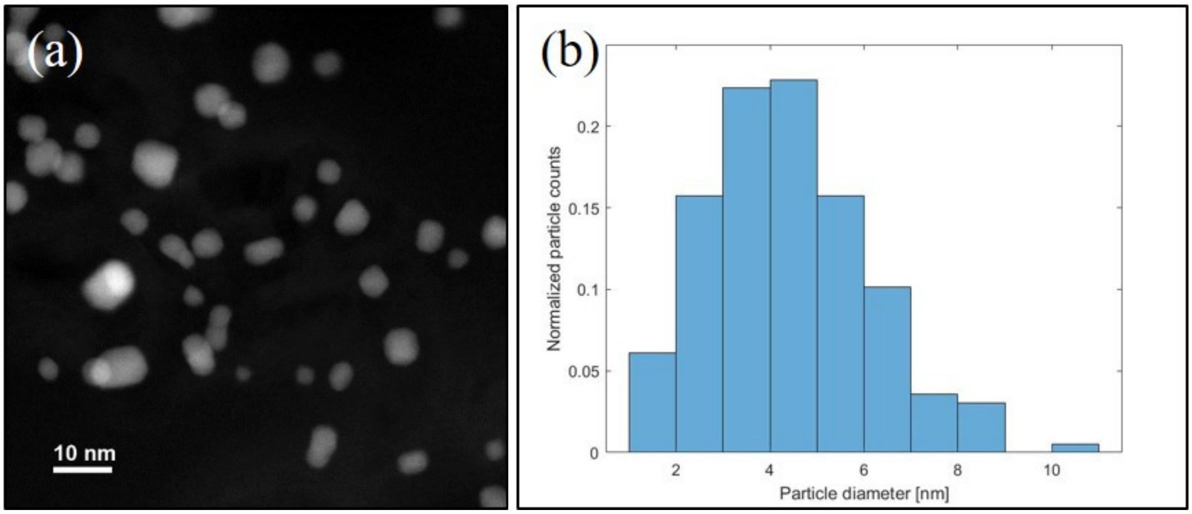

Figure 3: a) HAADF-STEM image of the Pt nanoparticles. b) Normalized platinum particle size histogram.

From HRTEM images, an averaged Nafion thickness is extracted. In figure 4, a representative HRTEM image of the cathode cross-section cut by cryo-ultramicrotomy is presented. This image shows that the primary carbon nanoparticles - with 25 nm in diameter - that support the dark Pt nanoparticles are hollow nanoparticles. The shell of these carbon particles, which consists of graphitic planes, is about 3 nm-thick. This hollow structure was clearly revealed in an electron tomography experiment performed on a similar catalyst [58]. In this same image (fig. 4), the Nafion is identifiable by its typical contrast of amorphous material. Although the ionomer does not cover homogeneously all the carbon nanoparticles, a thin Nafion layer approximately 6 to 8 nm-thick is often observed surrounding the carbon nanoparticles which is in agreement with the electron tomography analysis [65]. To have a better description of the Nafion distribution, an electron tomography experiment is required. However, from the HRTEM images, an average thickness can be extracted by performing multiple measurements in different regions of the image. In the end, an average value of 8 nm was found for the Nafion thickness.

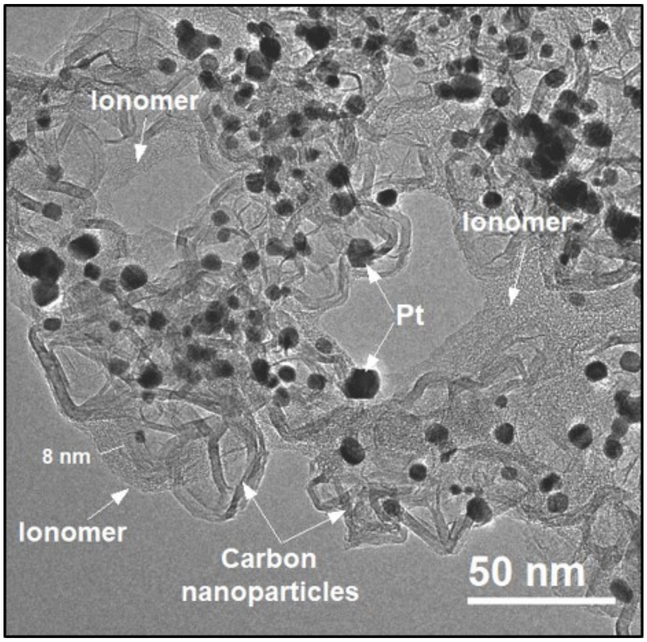

Figure 4: HRTEM image where Nafion is observed around the Pt/C agglomerates.

For the solid phase obtained on the segment FIB-SEM image stack, the assumption of assigning that phase as carbon was taken (a valid assumption as long as the platinum volume is far lower than the carbon one), while the platinum nanoparticles were later randomly distributed on its surface and the Nafion thin layer was placed uniformly around the agglomerates as explained in section 4 of this article. A structure with an I/C and a Pt loading of 1 and 0.3 $mg \cdot cm^{-2}$ respectively was obtained and the composition was found to be in accordance with experimentally measured data. To determine the Pt loading, the FIB-SEM image stack was assumed to be a repetitive unit along the catalyst layer thickness. At this stage, other works assumed a single carbon/platinum phase [20], which does not allow to capture the effects of particle distribution on structure performance as it is reported in section 5 of this work and will be described in more detail in our future publication.

Regarding the pore phase, all the pores were found to be connected - when just considering the FIB-SEM image stack - as already shown by [47]. The porosity value obtained from the segmented FIB-SEM volume was 55%. Here, an evaluation of the pore size distribution on the post-treated FIB-SEM output stack following the method of maximum sphere inscription (MSI) was performed [69]. When comparing the obtained pore size distribution (PSD) (fig. 5) with the one from [70] - where a CCL with a similar carbon support and composition except for a platinum/carbon weight ratio (46 wt%) - it is possible to observe that the pore size peak location found in this work - 38 nm - is slightly shifted from the one found by [70] - 50 nm - using mercury porosimetry. Such shift (also observed by [26]) can be associated with limitations of the MIP technique itself as it does not allow determining the smallest pores and it possesses a destructive nature which may introduce additional artifacts by changing the structure. This argument also explains some pore sizes beyond 150 nm that were found in the work of [70]. The impact of ionomer content over the pore size distribution has been already reported by [71] on a CL with Pt/KB and it was found that increasing the ionomer content beyond 30% implies a very significant decrease in pore size. When comparing the PSD to the one of a catalyst layer using a catalyst from the same manufacturer [29] though with a different Pt loading (50.6 wt%), a similar pore size distribution is also found.

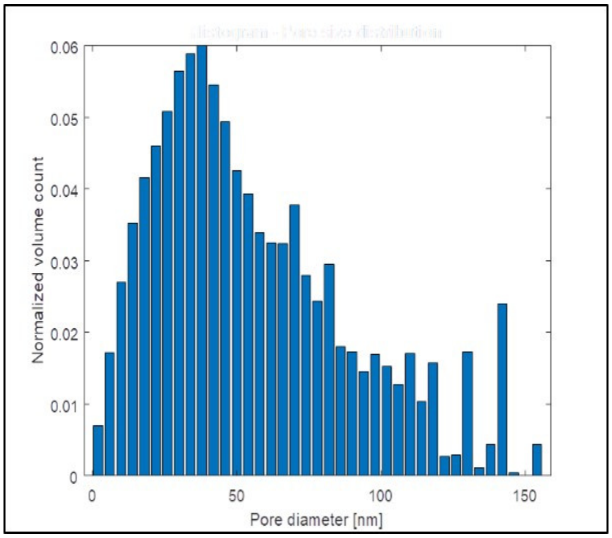

Figure 5: Histogram - Pore size distribution.

Transforming the post-treated data into a proper geometry for numerical modeling is the following step. This step will be described thoroughly in the following section - 4.

4. Geometry building

Comsol ® Multiphysics requires a CAD geometry in order to produce a mesh and perform numerical calculations involving physical phenomena such as gas transport, heat transfer and electrochemical reactions. Since reconstructed segmented images cannot be directly introduced for performing CFD simulations, different methods must be adopted. The main idea behind the method proposed in this work lies on placing parallelepiped/cubic-shaped solids in the positions of bitmap voxels that hold 'true' logical values. In order to attain the final geometry, four main steps must be accomplished:

- building the carbon phase;
- adding platinum spheres to the carbon surface;
- adding a 'uniform' Nafion thin layer around the Pt/C agglomerates;
- adding the pore phase.

The geometry reproduced on Comsol ® Multiphysics is illustrated in figure 6 - from the selected portion of the raw image stack to the final geometry. The procedure adopted was chosen over direct mesh importation since it allows differentiating the phases within the structure. It is then worth noting that adding the platinum and Nafion phases directly on a mesh is not possible.

4.1. Carbon phase building

The process of moving from segmented images to numerical simulation (fig. 6) starts with the importation of the post-treated FIB-SEM image stack to MATLAB® and proceeds with the conversion onto a binary map ('1' is assigned to the solid phase and '0' to the void). Here, the assumption of assigning that solid phase as carbon was taken (a valid assumption as long as the platinum volume is far lower than the carbon one). The transition from the portion of the carbon binary map stack (fig. 6b) to the 3D structure (fig. 6c) in the numerical software could be established through placing voxel-size cubic blocks in space according to the distribution of the 'true' logical values ('1'), but this procedure would turn extremely time costly. A solution to the issue could be locating and placing parallelepiped/cubic-shaped solids (larger than the voxel's dimensions) by descending order of size. Still, this procedure may take long and so a slightly modified version of this method is adopted:

1. Disassemble the binary map stack [P,Q,R] into N stacks of equal size $[P^i, Q^i, R^i]...[P^N, Q^N, R^N]$ (where N is arbitrarily defined on the restricted set $\{N \in \mathbb{N} \mid \frac{length(P)}{length(P^i)} \in \mathbb{N} \wedge \frac{length(Q)}{length(Q^i)} \in \mathbb{N} \wedge \frac{length(R)}{length(R^i)} \in \mathbb{N}\}$);
2. For each of the N stacks, read and list the matrix indexes holding 'true' logical values;
   (a) Find the largest solid (parallelepiped/cubic shape) that can be built departing from each of the indexes of step 2 and store the respective coordinates and size;
   (b) Convert the 'true' logical values included in the solid found into 'false' logical values;
   (c) Return to step 2a until all the solids within $[P^i, Q^i, R^i]$ are found;
   (d) Read the next submatrix (i = i + 1) and return to step 2 until (i > N).
3. Place the blocks listed in step 2a according to the assigned size and position.
4. Perform a boolean operation - 'union' - between all the built blocks. The result is presented in figure 6c.

This means that the portion of FIB-SEM data transferred into the finite element software is exactly the same contained in the selected portion of the reconstructed FIB-SEM image stack.

4.2. Platinum phase building

Platinum nanoparticles under the assumption of spherically-shaped are randomly placed on the surface of the carbon support according to the size histogram (figure 3b). The procedure to do so is the following:

1. Randomly select a platinum nanoparticle size from the histogram (fig. 3b);
2. Randomly place the nanoparticle sphere on the carbon surface;
3. If the Pt/C mass ratio set - eq. (1) - is not satisfied return to step 1.
4. Perform a boolean operation - 'difference' - between the platinum and carbon phases so that the overlapped zone can be resolved. This region is assigned to the platinum phase (fig. 6d).

$$Pt/C_{massratio} = \frac{\rho_{Pt}V_{Pt}}{\rho_{Pt}V_{Pt} + \rho_C V_C} \tag{1}$$

The boolean operations can be defined as logical operations (union, intersection, difference...) between domain sets in order to define a new domain set. Among the boolean operations performed, the ones which may be troublesome include the 'difference' operations between the platinum and carbon phase and between the platinum and ionomer phase (described in the following subsection), where a removal of a small volume of carbon and ionomer close to its surface is performed so that a platinum particle can be placed.

4.3. Nafion phase building

Finally, the Pt/C agglomerates are covered by a uniform Nafion thin film under the following procedure:

1. Duplicate the carbon matrix;
2. On the duplicated matrix, add 4 voxels with a 'true' logical value ('1') in the normal direction to every interface between '1' and '0' throughout the matrix;
3. Subtract the duplicated matrix, which comprises both carbon and Nafion, to the carbon matrix. The remaining 'true' logical values in the matrix represent the Nafion;
4. Perform steps 1 to 4 of the carbon phase building on the Nafion matrix;
5. Perform a boolean operation - 'difference' - between the Nafion and platinum phases so that the overlapped zone can be resolved by assigning it to the platinum phase. The result is presented in figure 6e.

Here, the Nafion layer is assumed to have a constant averaged-thickness as assumed in [6, 35, 49]. This averaged-thickness is extracted from the Nafion observation on 2D HRTEM images. However, atomic simulations indicate that ionomer cannot penetrate into the primary pores [72, 73]. This can be an important factor to take into account in the development of more realistic geometries with a heterogeneous Nafion layer coverage. When placing the uniform Nafion thin layer, small isolated pores are observed, though these are assumed to be negligible as these appear in a residual quantity and are 2-4 nm sized.

4.4. Pore phase building

In order to complete the geometry, the pore phase must be added. To do so, the following procedure is adopted:

1. Perform steps 1 to 4 of the carbon phase building on the matrix comprising both carbon and Nafion phases with the unique difference that the terms 'true' and 'false' mentioned in the operations of steps 2 and 2b must be read as 'false' and 'true' respectively. The final result is presented in figure 6f.

The algorithm builds the primary and the secondary pores separately, opening the possibility to distinguish among them for further improvements of the model, such as taking into account liquid water flooding. Here, primary and secondary pores are defined as in the work of Mashio et al. [74], with the former corresponding to pores smaller than 10 nm and the latter to pores larger than 10 nm.

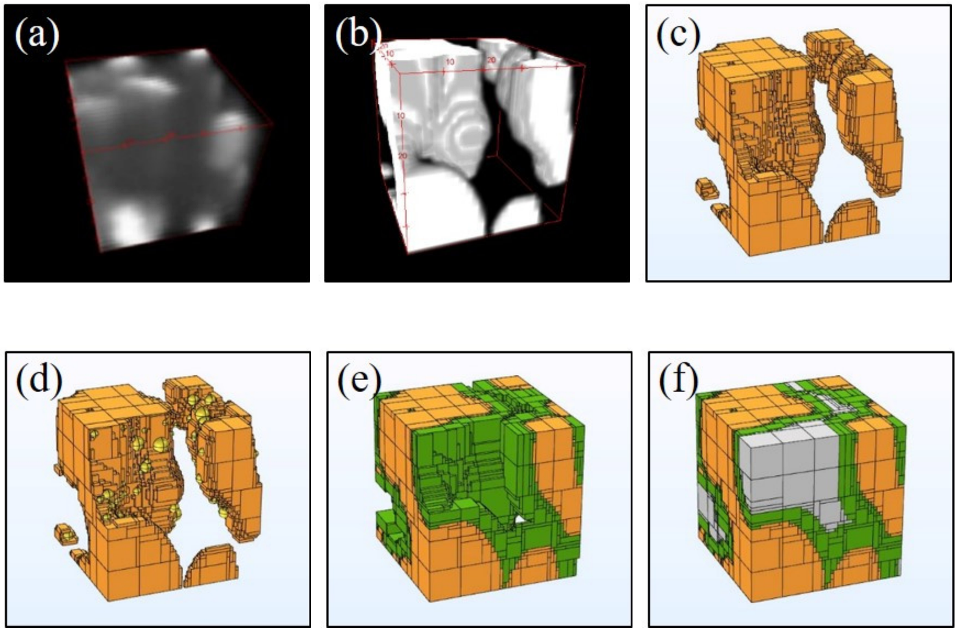

Figure 6: a) Raw FIB-SEM stack portion of [100*100*100] nm. b) Corresponding segmented stack portion. c) Corresponding reconstructed carbon phase. d) Carbon phase with platinum particles distributed on the surface. e) Addition of a ionomer layer over the Pt/C agglomerate. f) Addition of the pore phase. Legend: gray: pore phase; green: ionomer phase; orange: carbon phase; yellow: platinum phase).

It is important to note that when attempting to reproduce geometries of significantly large dimensions ($10^2 \sim 10^3$ nm), the process becomes extremely time intensive. So, due to the need of maintaining a reasonable reconstruction time and also due to computer power and software limitations - the incapability to solve booleans for a high number of intersecting features - the size selected for the geometries over which numerical calculations were performed (reported in section 5) was [100*100*100] nm. This was found to be enough for the purpose of this work as it allows to capture the effects of the heterogeneities at such a local scale. Furthermore, the effects of these heterogeneities will be extended to performance evaluation studies over the whole catalyst layer thickness, which will be reported in a future article.

In the following section, a description of the physical model will be presented along with some numerical results output from the study of two different geometries.

5. Numerical model description and results

In this work, a model was developed and simulations on agglomerate geometries extracted from different zones within the sample were performed. A short description of this model is presented in the sections below. Since the model requires certain local conditions (species concentrations, fluxes and ionic potential) as an input, a coupling with a macroscale MEA model [17] is established. Moreover, the CCL region selected to extract these conditions was one close to the CCL/MB interface since a higher current density and a low oxygen concentration are expected.

5.1. Model

The physical model adopted in this work is based on the work of Randrianarizafy et al. [17], with the inclusion of a 4-step reaction mechanism to describe the oxygen reduction reaction [3]. A summary of this model is presented in table 1. Additionally, further details can be found in the works aforementioned.

	Ionic transport (N)	O_2 transport (N)	O_2 transport (P)
Governing equations	$\nabla \cdot (-\kappa \nabla \varphi) = 0$	$\nabla \cdot (-D_{O_2,N} \nabla C_{O_2,N}) = 0$	$\nabla \cdot (-D_{O_2,P} \nabla C_{O_2,P}) = 0$
Nafion inlet	$\varphi_{in} = \varphi^*$; $\kappa \frac{\partial \varphi}{\partial n} \vert_{in} = flux_{H^+}$	$D_{O_2,N} \frac{\partial C_{O_2}}{\partial n} = 0$	$-$
Nafion outlet	$-$	$-$	$-$
Nafion/Pt interface	$\kappa \frac{\partial \varphi}{\partial n} = -(j_{RA} + j_{RT} + j_{RD})$	$D_{O_2,N} \frac{\partial C_{O_2,N}}{\partial n} = -\frac{j_{DA}+j_{RA}}{2F}$	$-$
Nafion/C interface	$\kappa \frac{\partial \varphi}{\partial n} = 0$	$D_{O_2,N} \frac{\partial C_{O_2}}{\partial n} = 0$	$-$
Nafion/Pore interface	$\kappa \frac{\partial \varphi}{\partial n} = 0$	$C_{O_2,N/P} = C_{O_2,P} RT H_{O_2,N}$	$D_{O_2,P} \frac{\partial C_{O_2,P}}{\partial n} = D_{O_2,N} \frac{\partial C_{O_2,N}}{\partial n}$
Pore inlet	$-$	$-$	$C_{O_2,in} = C^*_{O_2}$; $D_{O_2,P} \frac{\partial C_{O_2,P}}{\partial n} \vert_{in} = flux_{O_2,P}$
Pore outlet	$-$	$-$	$-$
Dissociate adsorption	$j_{DA} = j^* a_{O_2}^{1/2} \exp\left(\frac{-\triangle G^*_{DA}}{k_B T}\right) \theta_{Pt} - j^* \exp\left(\frac{-\triangle G^*_{-DA}}{k_B T}\right) \theta_{O,ads}$		
Reductive adsorption	$j_{RA} = j^* a_{O_2}^{1/2} a_{H^+} \exp\left(\frac{-\triangle G^*_{RA}}{k_B T}\right) \theta_{Pt} - j^* \exp\left(\frac{-\triangle G^*_{-RA}}{k_B T}\right) \theta_{OH,ads}$		
Reductive transition	$j_{RT} = j^* a_{H^+} \exp\left(\frac{-\triangle G^*_{RT}}{k_B T}\right) \theta_{O,ads} - j^* \exp\left(\frac{-\triangle G^*_{-RT}}{k_B T}\right) \theta_{OH,ads}$		
Reductive desorption	$j_{RD} = j^* a_{H^+} \exp\left(\frac{-\triangle G^*_{RD}}{k_B T}\right) \theta_{OH,ads} - j^* \exp\left(\frac{-\triangle G^*_{-RD}}{k_B T}\right) \theta_{Pt}$		
Forward DA	$\triangle G^*_{DA} = \triangle G^{\circ}_{DA}$	Backward DA	$\triangle G^*_{-DA} = \triangle G^{\circ}_{DA} - \triangle G^{\circ}_{O}$
Forward RA	$\triangle G^*_{RA} = \triangle G^{\circ}_{RA} + \beta e \eta$	Backward RA	$\triangle G^*_{-RA} = \triangle G^{\circ}_{RA} - \triangle G^{\circ}_{OH} - \beta e \eta$
Forward RD	$\triangle G^*_{RD} = \triangle G^{\circ}_{RD} + \beta e \eta$	Backward RD	$\triangle G^*_{-RD} = \triangle G^{\circ}_{RD} + \triangle G^{\circ}_{OH} - \beta e \eta$
Forward RT	$\triangle G^*_{RT} = \triangle G^{\circ}_{RT} + \beta e \eta$	Backward RT	$\triangle G^*_{-RT} = \triangle G^{\circ}_{RT} - \triangle G^{\circ}_{OH} + \triangle G^{\circ}_{O} - \beta e \eta$
O2 activity	$a_{O_2} = \frac{C_{O_2}}{C^{\circ}_{O_2}}$	Proton activity	$a_{H^+} = \frac{\lambda_{HR=100\%}}{\lambda_{HR}}$ (ref. [17])
Transport parameters			
Ionic conductivity	$\kappa = 100 \cdot (0.005139\lambda - 0.00326) \cdot \exp\left(1268 \cdot \left(\frac{1}{303} - \frac{1}{T}\right)\right)$ (ref. [75])		
O2 diffusivity (N)	$D_{O_2,Naf} = \overline{D_{O_2,Nafpore}(\lambda) + D_{O_2,Nafbulk}(\lambda) + D_{O_2,Nafplatinum}(\lambda)} \exp\left(-2768 \left(\frac{1}{T} - \frac{1}{303}\right)\right)$ (ref. [76])		
O2 diffusivity (P)	$D_{O_2,Pore} = \frac{1}{D^{-1}_{Kn} + D^{-1}_{O_2/N_2}(P,T)}$, with $D_{Kn} = \frac{d}{3}\sqrt{\frac{8RT}{\pi M_{O_2}}}$		
Electrochemical parameters		Electrochemical parameters	
$\triangle G^{\circ}_{DA}$	$0.313[eV]$	$\triangle G^{\circ}_{RA}$	$0.487[eV]$
$\triangle G^{\circ}_{RD}$	$0.222[eV]$	$\triangle G^{\circ}_{RT}$	$0.472[eV]$
$\triangle G^{\circ}_{O}$	$-0.274[eV]$	$\triangle G^{\circ}_{OH}$	$-0.301[eV]$
β	0.5	j^*	$1000[A \cdot cm^{-2}]$
Relations			
D_{O_2/N_2}	$6.43 \cdot 10^{-5} \frac{T^{1.823}}{P} [m^2 \cdot s^{-1}]$		

Table 1: Model description and used parameters. Here, the letters (N) and (P) are used to refer to the Nafion and pore phases.

It is worth mentioning that both ionic ($flux_{H^+}$) and oxygen boundary fluxes ($flux_{O_2,P}$) in the Nafion and pore phases respectively, as well as ionic potential (φ^*) and oxygen concentration ($C^*_{O_2}$) are extracted from the MEA scale model.

5.2. Results and discussion

In this work, two different geometries are selected as examples to perform numerical calculations with the objective of studying the effects of structure heterogeneities on the local performance. These numerical calculations are performed on Comsol ® Multiphysics. The reason behind the choice of these geometries - structure 1 (fig. 7a) and structure 2 (fig. 7f) - is that these presented more significant structure effects. These effects include severe oxygen mass transport losses in the Nafion phase and slight interparticle competition effects [77]. While the former arises from the difficulty for oxygen to cross the Nafion film and is reportedly amplified with an increase in relative humidity [76], the latter arises from the competition for oxygen consumption between particles. This platinum interparticle competition phenomenon takes place when oxygen mass transport through the Nafion film is limiting. In addition, this effect is amplified as the distance between platinum particles is shortened (figs. 7c and 7h).

For all these geometries/structures, a pre-defined tetrahedral mesh containing over around 600,000 elements and resulting in a number of degrees of freedom of up to ~ 2,800,000 is adopted. Though, only the pore and Nafion domains are meshed, since the set of physics defined in the preceding subsections is only applied in these domains. When analyzing the structures, it is possible to observe at least one region in structure 1 (left bottom corner of figure 7a) and another in structure 2 (right top corner of figure 7f) with the presence of a large Nafion agglomerate with a reduced Nafion/pore interface. This may lead to severe mass transport losses in those regions as it is discussed further in this subsection. Also, in both structures, the carbon surface is quite low, and since the Pt/C is held constant for every geometry, a reduced Pt interparticle distance relatively to other structures is obtained. In order to collect further information on how the structure may impact the local performance, profiles referring to the oxygen concentration distribution in the pore and Nafion phases, and to the current density distribution on the surface of the Pt particles are presented and discussed. The distribution of these variables of interest - oxygen concentration on the pore and Nafion phases and current density per catalytic surface in two different views (global and detailed views) - for both structures 1 and 2 are illustrated in figures 7b-e and figures 7g-j. Moreover, the ionic potential distribution is not further investigated in this study, once negligible losses are observed at this scale independently of the geometry. Though, these losses become important when upscaling to the whole CL layer thickness.

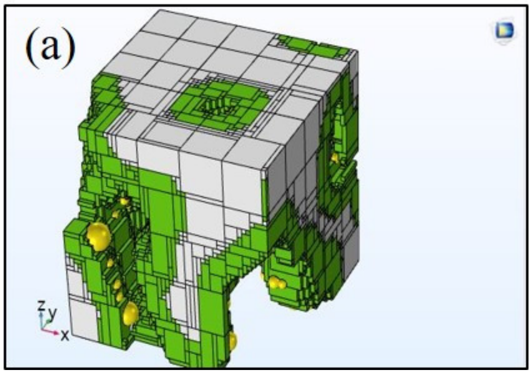
(a)
z
y
x

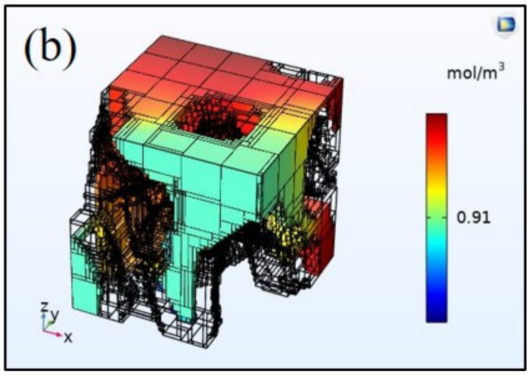
(b)
mol/m^3
0.91
z
y
x

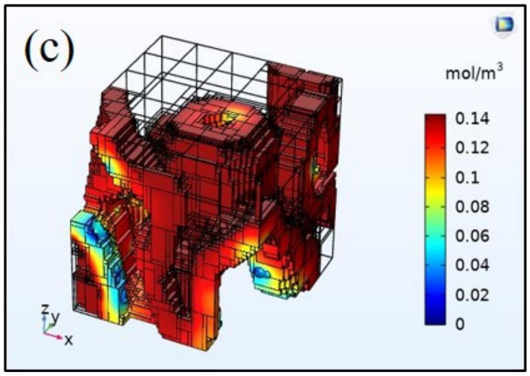
(c)
mol/m^3
0.14
0.12
0.1
0.08
0.06
0.04
0.02
0
z
y
x

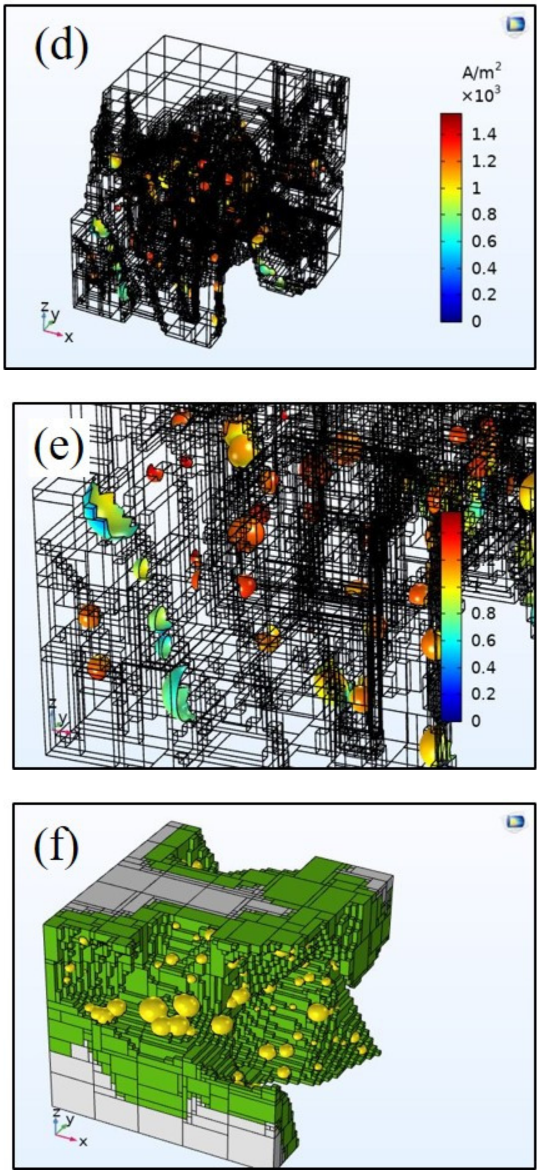
(d)
A/m²
×10³
1.4
1.2
1
0.8
0.6
0.4
0.2
0
z y
x
(e)
0.8
0.6
0.4
0.2
0
z y
(f)
z y
x

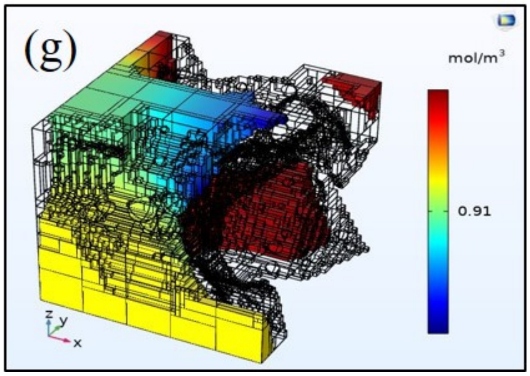
(g)
mol/m^3
0.91
z
y
x

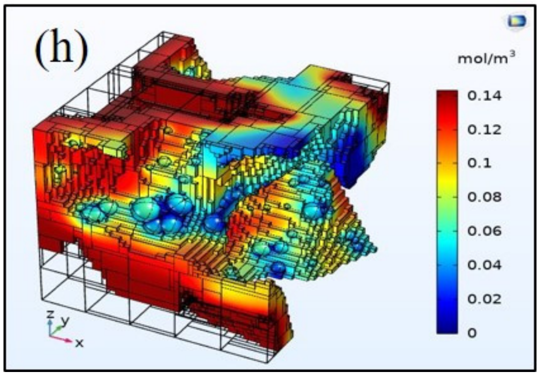
(h)
mol/m^3
0.14
0.12
0.1
0.08
0.06
0.04
0.02
0
z
y
x

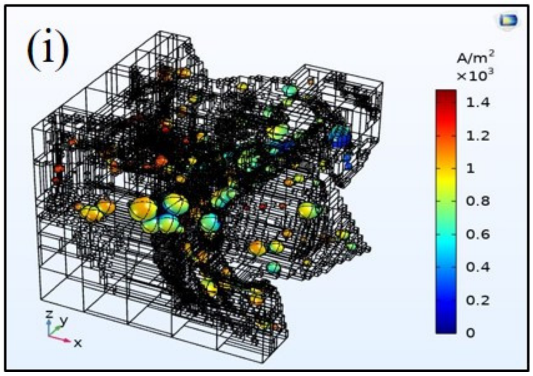
(i)
A/m^2
×10^3
1.4
1.2
1
0.8
0.6
0.4
0.2
0
z
y
x

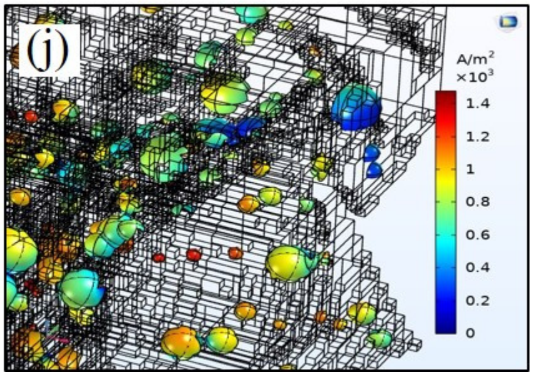

Figure 7: Performance analysis for two different geometries. For structure 1: a) geometry of the structure. b) oxygen concentration on the pore phase (in $mol \cdot m^{-3}$) . c) oxygen concentration on the ionomer phase (in $mol \cdot m^{-3}$) . d) current density per catalytic surface (in $A \cdot m_{Pt}^{-2}$). e) detailed view: current density per catalytic surface. For structure 2: f) geometry of the structure. g) oxygen concentration on the pore phase. h) oxygen concentration on the ionomer phase. i) current density per catalytic surface. j) detailed view: current density per catalytic surface. Legend of figures 7a and 7f: gray: pore phase; green: ionomer phase; yellow: platinum phase)

On the figures 7b and 7g it is possible to observe the oxygen concentration profiles in the pore phase for structures 1 and 2 respectively. These profiles indicate that oxygen concentration gradients are negligible for both cases. Furthermore, these are related to the fact that the analyzed geometries represent a very small portion of the catalyst layer - [100*100*100] nm - and that the zone under study is located next to the membrane where low oxygen fluxes are crossing the pore phase. In addition, it is important to refer that the amplitude of the oxygen transport losses in the pore phase is expected to significantly increase with the decrease in pore size as Knudsen effects become more significant. It is also worth noting that the oxygen concentration gradient is naturally expected to be higher the closer to the gas diffusion layer - where higher oxygen fluxes are found. Therefore, a possible path to minimize the oxygen transport losses would be to favor the location of larger pores in these areas.

On the figures 7c and 7h, the oxygen concentration profiles in the Nafion phase of both structure 1 and 2 are presented. Unlike the oxygen concentration profiles in the pore phase, here, severe oxygen diffusion limitations are observed. This is expected as the oxygen diffusivities in both phases can differ up to ~ 4-5 orders of magnitude. In structure 1, it is possible to observe a region of oxygen starvation (bottom left corner of fig. 7c). When looking in parallel to the same region in figure 7d, where the current density profile on the surface of the platinum particles is presented, one can observe that the platinum particles there located are fairly less active than other particles (i.e. present a lower current density). This is linked to the high oxygen diffusion resistance through the Nafion layer (as a result of a low ratio of pore/Nafion surface to Nafion agglomerate volume) and possibly to a platinum interparticle competition effect. A clearer identification of the effects can be performed when analyzing the oxygen concentration profile in the Nafion phase of structure 2 (figure 7h). In the corresponding figure, interesting patterns indicating the occurrence of interparticle competition effects emerge. Here, multiple zones can be observed where a relatively low oxygen concentration in the ionomer seems to be coupled with an effect of the Pt interparticle distance. In fact, the particles which are relatively close to each other present a slightly lower concentration in between them when comparing to the surroundings. Therefore, it can be concluded that platinum interparticle competition effects appear to play a role in performance - as reported by [21, 77] - when in the presence of regions with relatively low oxygen concentration. In addition, when looking at the right top corner of the structure presented in figure 7h, a large region with a low oxygen concentration stands out. When looking also at figure 7g, one can observe a weak pore contact (reduced pore/Nafion interface) in that same Nafion agglomerate. As a result, it can already be concluded that severe mass transport limitations occur in large Nafion agglomerates and that these can be optimized through reducing the Nafion agglomerate sizes and improving the pore network. Additionally, it can be stated that it is crucial to have an accurate picture of the Nafion layer distribution as it appears to highly impact the performance of a CCL.

On the figures 7d and 7i, the profiles of current density per unit Pt surface of both structure 1 and 2 are presented. More detailed views of these are presented in figures 7e and 7j. On both figures 7d and 7i, significant current density heterogeneities are observed, in addition to particles with severe underutilization. Such current density profiles appear to be directly linked to the oxygen concentration profiles as the current density varies in proportion to the oxygen concentration in that region. Therefore, it can be concluded that oxygen transport limitations highly dictate the Pt utilization. In order to better comprehend these heterogeneities, histograms of current density distribution on normalized Pt particle surface are presented in figures 8a and 8b. Furthermore, the data presented in these figures refers to the averaged current density of each particle normalized on its surface. While for structure 1 the current density peak is located in the interval of 1000-1100 $A \cdot m_{Pt}^{-2}$, for structure 2 it is slightly shifted to lower values, in the interval of 700-800 $A \cdot m_{Pt}^{-2}$. In both cases, it is observed that more than 50% of the Pt surface outputs a mean current density between 800 and 1200 $A \cdot m_{Pt}^{-2}$. However, significant differences emerge when looking at less active Pt particles. By less active it is meant lower current density production. In the case of structure 1, it is found that most Pt surface outputs a current density above 800 $A \cdot m_{Pt}^{-2}$. Though, a different scenario is observed in case of structure 2 since nearly 41% of the Pt particles are found to produce a current density ranging between 200 and 800 $A \cdot m_{Pt}^{-2}$. As stated above, this is clearly linked to the degree of access of these particles to oxygen. In order to compare the overall platinum utilization - defined as current density per Pt surface - of both structures, the global mean current density per catalytic surface is computed, with the structure 1 having an utilization 22% higher than structure 2. Both Pt utilizations are expected to improve with the optimization of the platinum interparticle distance and the pore network. In conclusion, it is reasonable to state that understanding the cathode catalyst layer structure is crucial in order to accurately predict the current density distribution and performance.

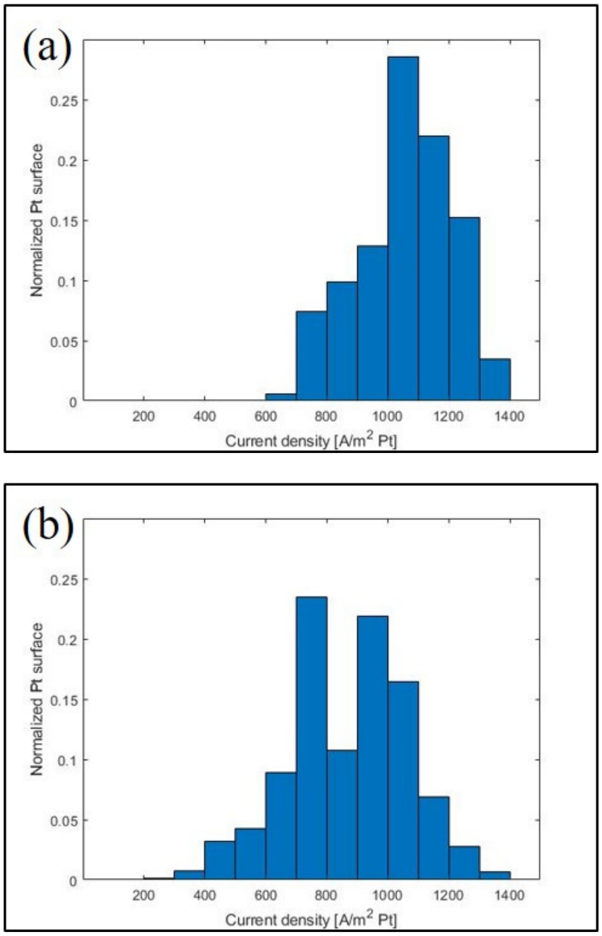

Figure 8: Dispersion of current density per catalytic surface. a) structure 1. b) structure 2.

6. Conclusion

The approach presented in this work demonstrated to be an appropriate tool for computationally efficient geometry building, numerical simulation and for highlighting the effect of important features within the catalyst layer which already emerge at a nanoscale. Here, a method for the generation of 3D cathode catalyst layer geometries was presented. These geometries were generated out of portions from a FIB-SEM [2.178*0.972*2] μm image stack which was assumed to be representative of the whole extension of the cathode catalyst layer. Prior to the geometry build-up, the FIB-SEM image stack was aligned and segmented using criteria beyond pixel intensity such as pattern recognition. Since it was not possible to accurately measure the Pt particle size from FIB-SEM images due to the low resolution, multiple HAADF-STEM images were used in order to extract the Pt particle size. From these images, a representative particle size histogram was obtained and the particles were distributed on the surface of the carbon support accordingly.

The Nafion phase was analyzed using HRTEM images, from which an average thin film thickness was extracted. A Nafion thin layer was then placed uniformly all over the Pt/C agglomerates. Using this procedure, two different geometries were built and numerical simulations were performed. Moreover, performance studies on the two different geometries demonstrated how crucial it is to perform a full phase discretization (carbon, platinum, Nafion and pore phase) when performing agglomerate/pore scale simulations which could otherwise lead to wrong interpretations. These studies also provide some insights on how structural features - the platinum particle distribution, pore tortuosity and size, Nafion layer thickness - impact the performance at the agglomerate scale. From analyzing the results, it can be concluded that it is paramount to understand the Pt particle distribution over the carbon support as already reported by [21, 77] at least in cases of relatively low oxygen concentration at the Pt surface. It is also found that significant current density distribution heterogeneities on the Pt particle surface are present at the scale of [100*100*100] nm. Another important conclusion is that oxygen diffusion in the ionomer is the main source of mass transport losses, which is in accordance with the conclusions of [6, 78].

One of the perspectives for future development over the structural reconstruction method presented is to define a 2-point correlation function output from 3D-TEM tomography on an agglomerate and place platinum particles accordingly instead of randomly distributing these on the carbon surface. Another perspective consists in heterogeneously distributing Nafion by covering the zones in contact with secondary pores (pores larger than 10 nm as defined in the work of Mashio et al. [74]), as atomic simulations indicate that Nafion cannot penetrate in the primary pores [72, 73].

The extension of this agglomerate scale to the catalyst layer scale along with the agglomerate/pore scale and macroscale model coupling is ongoing and will be reported in a future article.

Acknowledgments

The authors want to acknowledge Christine Nayoze for preparing the CCM used in this work.

References

[1] J. Benziger, E. Kimball, R. Mejia-Ariza, I. Kevrekidis, Oxygen mass transport limitations at the cathode of polymer electrolyte membrane fuel cells, AIChE 57 (9) (2010) 2505–2517.

[2] J. Wang, J. Zhang, R. Adzic, Double-trap kinetic equation for the oxygen reduction reaction on pt(111) in acidic media, J. Phys. Chem. A 111 (49) (2007) 12702–12710.

[3] M. Moore, A. Putz, M. Secanell, Investigation of the orr using the double-trap intrinsic kinetic model, J. Electrochem. Soc. 160 (6) (2013) 670–681.

[4] M. Sassin, Y. Garsany, R. A. III, R. Hjelm, K. Swider-Lyons, Understanding the interplay between cathode catalyst layer porosity and thickness on transport limitations en route to high-performance pemfcs, Int. J. Hydrogen Energy 44 (31) (2019) 16944–16955.

[5] K. Kudo, R. Jinnouchi, Y. Morimoto, Humidity and temperature dependences of oxygen transport resistance of nafion thin film of platinum electrode, Electrochim. Acta 209 (2016) 682–690.

[6] M. Sabharwal, L. Pant, A. Putz, D. Susac, J. Jankovic, M. Secanell, Analysis of catalyst layer mcirostructures: from imaging to performance, Fuel Cells 16 (6) (2016) 734–753.

[7] K. Kudo, T. Suzuki, Y. Morimoto, Analysis of oxygen dissolution rate from gas phase into nafion surface and development of an agglomerate model, ECS Trans. 33 (1) (2010) 1495–1502.

[8] S. DeCaluwe, A. Baker, P. Bhargava, J. Fischer, Structure-property relationships at nafion thin-film interfaces: Thickness effects on hydration and anisotropic ion transport, Nano Energy 46 (2018) 91–100.

[9] D. Paul, K. Karan, Conductivity and wettability changes of ultrathin nafion films subjected to thermal annealing and liquid water exposure, J. Phys. Chem. C 118 (4) (2014) 1828–1835.

[10] D. Paul, R. McCreery, K. Karan, Proton transport property in supported nafion nanothin films by electrochemical impedance spectroscopy, J. Electrochem. Soc. 161 (14) (2014) 1395–1402.

[11] D. W. III, J. Chlistunoff, J. Majewski, R. Borup, Nafion structural phenomena at platinum and carbon interfaces, J. Am. Chem. Soc. 131 (50) (2009) 18096–18104.

[12] D. D. Borges, A. Franco, K. Malek, G. Gebel, S. Mossa, Inhomogeneous transport in model hydrated polymer electrolyte supported ultrathin films, ACS Nano 7 (8) (2013) 6767–6773.

[13] J. Aochi, T. Mabuchi, T. Tokumasu, Molecular dynamics study on proton transport in supported nafion ionomer thin films on lennard-jones walls, ECS Trans. 75 (14) (2016) 607–614.

[14] G. Hu, G. Li, Y. Zheng, Z. Zhang, Y. Xu, Optimization and parametric analysis of pemfc based on an agglomerate model for catalyst layer, J. Energy Inst. 87 (2) (2014) 163–174.

[15] S. Kamarajugadda, S. Mazumder, Generalized flooded agglomerate model for the cathode catalyst layer of a polymer electrolyte membrane fuel cell, J. Power Sources 208 (2012) 328–339.

[16] S. Li, J. Yuan, G. Xie, B. Sunden, Effects of agglomerate model parameters on transport characterization and performance of pem fuel cells, Int. J. Hydrogen Energy 43 (17) (2018) 8451–8463.

[17] B. Randrianarizafy, P. Schott, M. Chandesris, M. Gerard, Y. Bultel, Design optimization of rib/channel patterns in a pemfc through performance heterogeneities modelling, Int. J. Hydrogen Energy 43 (18) (2018) 8907–8926.

[18] L. Xing, M. Mamlouk, R. Kumar, K. Scott, Numerical investigation of the optimal nafion ionomer content in cathode catalyst layer: An agglomerate two-phase flow modelling, Int. J. Hydrogen Energy 39 (17) (2014) 9087–9104.

[19] N.K.H.Dalasm, M. Fesanghary, K. Fushinobu, K. Okazaki, A study of the agglomerate catalyst layer for the cathode side of a proton exchange membrane fuel cell: Modeling and optimization, Electrochim. Acta 60 (2012) 55–65.

[20] X. Zhang, Y. Gao, H. Ostadi, K. Jiang, R. Chen, A proposed agglomerate model for oxygen reduction in the catalyst of proton exchange membrane fuel cells, Electrochim. Acta 150 (2014) 320–328.

[21] F. Cetinbas, S. Advani, A. Prasad, A modified agglomerate model with discrete catalyst particles for the pem fuel cell catalyst layer, J. Electrochem. Soc. 160 (8) (2013) 750–756.

[22] X. Zhang, H. Ostadi, K. Jiang, R. Chen, Reliability of the spherical agglomerate models for catalyst layer in polymer electrolyte membrane fuel cells, Electrochim. Acta 133 (2014) 475–483.

[23] F. Cetinbas, R. Ahluwalia, N. Kariuki, V. Andrade, Hybrid approach combining multiple characterization techniques and simulations for microstructural analysis of proton exchange membrane fuel cell electrodes, J. Power Sources 344 (2017) 62–73.

[24] K. Karan, Pemfc catalyst layer: Recent advances in materials, microstructural characterization, and modeling, Curr. Opin. Electrochem. 5 (1) (2017) 27–35.

[25] A. Serov, M. Workman, K. Artyushkova, P. Atanassov, G. McCool, S. McKinney, H. Romero, B. Halevi, T. Stephenson, Highly stable precious metal-free cathode catalyst for fuel cell application, J. Power Sources 327 (2016) 557–564.

[26] M. Sabharwal, A. Putz, D. Susac, J. Jankovic, M. Secanell, Improving fib-sem reconstructions by using epoxy resin embedding, ECS Trans. 77 (11) (2017) 1337–1349.

[27] S. Stariha, K. Artyushkova, M. Workman, A. Serov, S. Mckinney, B. Halevi, P. Atanassov, Pgm-free fe-n-c catalysts for oxygen reduction reaction: Catalyst layer design, J. Power Sources (2016).

[28] M. Shojaeefard, G. Molaeimanesh, M. Nazemian, M. Moqaddari, A review on microstructure reconstruction of pem fuel cells porous electrodes for pore scale simulation, Int. J. Hydrogen Energy 41 (44) (2016) 20276–20293.

[29] S. Ghosh, H. Ohashi, H. Tabata, Y. Hashimasa, T. Yamaguchi, Microstructural pore analysis of the catalyst layer in a polymer electrolyte membrane fuel cell: A combination of resin pore-filling and fib/sem, Int. J. Hydrogen Energy 40 (45) (2015) 15663–15671.

[30] S. Vierrath, F. Guder, A. Menzel, M. Hagner, R. Zengerle, M. Zacharias, S. Thiele, Enhancing the quality of the tomography of nanoporous materials for better understanding of polymer electrolyte fuel cell materials, J. Power Sources 285 (2015) 413–417.

[31] T. Terao, G. Inoue, M. Kawase, N. Kubo, M. Yamaguchi, K. Yokoyama, T. Tokunaga, K. Shinohara, Y. Hara, T. Hara, Development of novel three-dimensional reconstruction method for porous media for polymer electrolyte fuel cells using focused ion beam-scanning electron microscope tomography, J. Power Sources 347 (2017) 108–113.

[32] H. Ishikawa, S. Henning, J. Herranz, A. Eychmuller, M. Uchida, T. Schmidt, Tomographic analysis and modeling of polymer electrolyte fuel cell unsupported catalyst layers, J. Electrochem. Soc. 165 (2) (2018) 7–16.

[33] A. Pournemat, H. Markotter, F. Wilhelm, S. Enz, H. Kropf, I. Manke, J. Scholta, Nano-scale monte carlo study on liquid water distribution within polymer electrolyte membrane fuel cell microporous layer, catalyst layer and their interfacial region, J. Power Sources 397 (2018) 271–279.

[34] H. Schulenburg, B. Schwanitz, J. Krbanjevic, N. Linse, R. Mokso, M. Stampanoni, A. Wokaun, G. Scherer, 3d imaging of polymer electrolyte fuel cell electrodes, ECS Trans. 33 (1) (2010).

[35] J. Jankovic, S. Zhang, A. Putz, M. Saha, D. Susac, Multiscale imaging and transport modeling for fuel cell electrodes, J. Mater. Res. 34 (4) (2019) 1–13.

[36] S. Babu, H. Chung, P. Zelenay, S. Litster, Resolving electrode morphology's impact on platinum group metal-free cathode performance using nano-ct of 3d hierarchical pore and ionomer distribution, ACS Appl. Mater. Interfaces 8 (48) (2016) 32764–32777.

[37] S. Ogawa, S. K. Babu, H. Chung, P. Zelenay, S. Litster, Direct simulations of coupled transport and reaction on nano-scale x-ray computed tomography images of platinum group metal-free catalyst cathodes, ECS Trans. 75 (14) (2016).

[38] J. Zhang, Y. Wang, J. Zhang, J. Liang, J. Lu, L. Xu, The effect of pt/c agglomerates in electrode on pemfc performance using 3d micro-structure lattice models, Int. J. Hydrogen Energy 42 (17) (2017) 12559–12566.

[39] W. Wu, F. Jiang, Microstructure reconstruction and characterization of pemfc electrodes, Int. J. Hydrogen Energy 39 (28) (2014) 15894–15906.

[40] K. Lange, P. Sui, N. Djilali, Pore scale modeling of a proton exchange membrane fuel cell catalyst layer: Effects of water vapor and temperature, J. Power Sources 196 (6) (2011) 3195–3203.

[41] M. Wang, M. Wang, N. Pan, S. Chen, Mesoscopic predictions of the effective thermal conductivity for microscale random porous media, Phys. Rev. E 75 (3) (2007) 36702.

[42] P. Mukherjee, C. Wang, Q. Kang, Mesoscopic modeling of two-phase behavior and flooding phenomena in polymer electrolyte fuel cells, Electrochim. Acta 54 (27) (2009) 6861–6875.

[43] S. Kim, H. Pitsch, Reconstruction and effective transport properties of the catalyst layer in pem fuel cells, J. Electrochem. Soc. 156 (6) (2009).

[44] W. Epting, J. Gelb, S. Litster, Resolving the three-dimensional microstructure of polymer electrolyte fuel cell electrodes using nanometer-scale x-ray computed tomography, Adv. Function. Mater. 22 (3) (2012) 555–560.

[45] R. White, D. Ramani, S. Eberhardt, M. Najm, F. Orfino, M. Dutta, E. Kjeang, Correlative x-ray tomographic imaging of catalyst layer degradation in fuel cells, J. Electrochem. Soc. 166 (13) (2019) 914–925.

[46] A. Pokhrel, M. E. Hannach, F. Orfino, M. Dutta, E. Kjeang, Failure analysis of fuel cell electrodes using three-dimensional multi-length scale x-ray computed tomography, J. Power Sources 329 (2016) 330–338.

[47] C. Ziegler, S. Thiele, R. Zengerle, Direct three-dimensional reconstruction of a nanoporous catalyst layer for a polymer electrolyte fuel cell, J. Power Sources 196 (4) (2011) 2094–2097.

[48] G. Inoue, K. Yokoyama, J. Ooyama, T. Terao, T. Tokunaga, Theoretical examination of effective oxygen diffusion coefficient and electrical conductivity of polymer electrolyte fuel cell porous components, J. Power Sources 327 (2016) 610–621.

[49] X. Zhang, Y. Gao, H. Ostadi, K. Jiang, R. Chen, Method to improve catalyst layer model for modelling proton exchange membrane fuel cell, J. Power Sources 289 (2015) 114–128.

[50] M. Okumura, Z. Noda, J. Matsuda, Y. Tachikawa, M. Nishihara, S. Lyth, A. Hayashi, K. Sasaki, Correlating cathode microstructure with pefc performance using fib-sem and tem, J. Electrochem. Soc. 164 (9) (2017) 928–934.

[51] S. Thiele, R. Zengerle, Nano-morphology of a polymer electrolyte fuel cell catalyst layer - imaging, reconstruction and analysis, Nano Res. 4 (9) (2011) 849–860.

[52] S. Thiele, T. Furstenhaupt, D. Banham, T. Hutzenlaub, V. Birss, C. Ziegler, R. Zengerle, Multiscale tomography of nanoporous carbon-supported noble metal catalyst layers, J. Power Sources 228 (2013) 185–192.

[53] E. Ambrosio, C. Francia, M. Manzoli, N. Penazzi, Platinum catalyst supported on mesoporous carbon for pemfc, Int. J. Hydrogen Energy 33 (12) (2008) 3142–3145.

[54] F. Nores-Pondal, I. Vilella, H. Troiani, M. Granada, S. de Miguel, O. Scelza, H. Conti, Catalytic activity vs size correlation in platinum catalysts of pem fuel cells prepared on carbon black by different methods, Int. J. Hydrogen Energy 34 (19) (2009) 8193–8203.

[55] K. More, R. Borup, K. Reeves, Identifying contributing degradation phenomena in pem fuel cell membrane electrode assemblies via electron microscopy, ECS Trans. 3 (1) (2006).

[56] C. Rao, B. Viswanathan, Monodispersed platinum nanoparticle supported carbon electrodes for hydrogen oxidation and oxygen reduction in proton exchange membrane fuel cells, J. Phys. Chem. C 114 (18) (2010) 8661–8667.

[57] E. Padgett, N. Andrejevic, Z. Liu, A. Kongkanand, W. Gu, K. Moriyama, Y. Jiang, S. Kumaraguru, T. Moylan, R. Kukreja, D. Muller, Connecting fuel cell catalyst nanostructure and accessibility using quantitative cryo-stem tomography, J. Electrochem. Soc. 165 (3) (2018).

[58] B. Sneed, D. Cullen, K. Reeves, O. Dyck, D. Langlois, R. Mukundan, R. Borup, K. More, 3d analysis of fuel cell electrocatalyst degradation on alternate carbon supports, ACS Appl. Mater. Interfaces 9 (35) (2017) 29839–29848.

[59] D. Cullen, R. Koestner, R. Kukreja, Z. Liu, S. Minko, O. Trotsenko, A. Tokarev, L. Guetaz, H. M. III, C. Parish, K. More, Imaging and microanalysis of thin ionomer layers by scanning transmission electron microscopy, J. Electrochem. Soc. 161 (10) (2014) 1111–1117.

[60] L. Guetaz, M. Lopez-Haro, S. Escribano, A. Morin, G. Gebel, D. Cullen, K. More, R. Borup, Catalyst-layer ionomer imaging of fuel cells, ECS Trans. 69 (17) (2015) 455–464.

[61] L. Melo, A. Hitchcock, Electron beam damage of perfluorosulfonic acid studied by soft x-ray spectromicroscopy, Micron 121 (2019) 8–20.

[62] D. Susac, V. Berejnov, A. Hitchcock, J. Stumper, Stxm study of the ionomer distribution in the pem fuel cell catalyst layers, ECS Trans. 41 (1) (2011).

[63] V. Berejnov, D. Susac, J. Stumper, A. Hitchcock, 3d chemical mapping of pem fuel cell cathodes by scanning transmission soft x-ray spectrotomography, ECS Trans. 50 (2) (2012) 361–368.

[64] J. Wu, L. Melo, X. Zhu, M. West, V. Berejnov, D. Susac, J. Stumper, A. Hitchcock, 4d imaging of polymer electrolyte membrane fuel cell catalyst layers by soft x-ray spectro-tomography, J. Power Sources 381 (2018) 72–83.

[65] M. Lopez-Haro, L. Guetaz, T. Printemps, A. Morin, S. Escribano, P. Jouneau, P. Bayle-Guillemaud, F. Chandezon, G. Gebel, Three-dimensional analysis of nafion layers in fuel cell electrodes, Nat. Commun. 5 (2014).

[66] T. Morawietz, M. Handl, C. Oldani, K. Friedrich, R.Hiesgen, Quantitative in situ analysis of ionomer structure in fuel cell catalytic layers, ACS Appl. Mater. Interfaces 8 (40) (2016) 27044–27054.

[67] T. Morawietz, M. Handl, C. Oldani, K. Friedrich, R. Hiesgen, Influence of water and temperature on ionomer in catalytic layers and membranes of fuel cells and electrolyzers evaluated by afm, Fuel Cells 18 (3) (2018) 239–250.

[68] S. Berg, D. Kutra, T. Kroeger, C. Straehle, B. Kausler, C. Haubold, M. Schiegg, J. Ales, T. Beier, M. Rudy, K. Eren, J. Cervantes, B. Xu, F. Beuttenmueller, A. Wolny, C. Zhang, U. Koethe, F. Hamprecht, A. Kreshuk, Ilastik: interactive machine learning for (bio)image analysis, Nat. Methods 16 (2019) 1226–1232.

[69] V. Novak, F. Stepanek, P. Koci, M. Marek, M. Kubicek, Evaluation of local pore sizes and transport properties in porous catalysts, Chem. Eng. Sci. 65 (7) (2010) 2352–2360.

[70] J. Shen, J. Zhou, N. Astrath, T. Navessin, Z. Liu, C. Lei, J. Rohling, D. Bessarabov, S. Knights, S. Ye, Measurement of effective gas diffusion coefficients of catalyst layers of pem fuel cells with a loschmidt diffusion cell, J. Power Sources 196 (2) (2011) 674–678.

[71] T. Soboleva, X. Zhao, K. Malek, Z. Xie, T. Navessin, S. Holdcroft, On the micro-, meso-, and macroporous structures of polymer electrolyte membrane fuel cell catalyst layers, ACS Appl. Mater. Interfaces 2 (2) (2010) 375–384.

[72] K. Malek, M. Eikerling, Q. Wang, T. Navessin, Z. Liu, Self-organization in catalyst layers of polymer electrolyte fuel cells, J. Phys. Chem. C 111 (36) (2007) 13627–13634.

[73] T. Mashio, K. Malek, M. Eikerling, A. Ohma, H. Kanesaka, K. Shinohara, Molecular dynamics study of ionomer and water adsorption at carbon support materials, J. Phys. Chem. C 114 (32) (2010) 13739–13745.

[74] T. Mashio, K. Sato, A. Ohma, Analysis of water adsorption and condensation in catalyst layers for polymer electrolyte fuel cells, Electrochim. Acta 140 (2014) 238–249.

[75] T. Springer, T. Zawodzinski, S. Gottesfeld, Polymer electrolyte fuel cell model, J. Electrochem. Soc. 138 (8) (1991) 2334–2341.

[76] Y. Kurihara, T. Mabuchi, T. Tokumasu, Molecular dynamics simulation of oxygen diffusivity, solubility and permeability in ionomer on pt surface, ECS Trans. 75 (14) (2016) 129–137.

[77] Y. Bultel, P. Ozil, R. Durand, Modelling of mass transfer within the pem fuel cell active layer: limitations at the particle level, J. Appl. Electrochem. 29 (9) (1999) 1025–1033.

[78] A. Kongkanand, M. Mathias, The priority and challenge of high-power performance of low-platinum proton-exchange membrane fuel cells, J. Phys. Chem. Lett. 7 (7) (2016) 1127–1137.

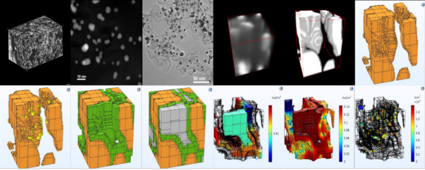
10 nm
50 nm
mol/m³
0.91
mol/m³
0.14
0.12
0.1
0.08
0.06
0.04
0.02
0
A/m²
×10⁵
1.4
1.2
1
0.8
0.6
0.4
0.2
0